

© 2017. This manuscript version is made available under the CC-BY-NC-ND 4.0 license <http://creativecommons.org/licenses/by-nc-nd/4.0/>

in compliance with the Elsevier Article Sharing Policy, available at:
<https://www.elsevier.com/about/our-business/policies/sharing>

The definitive version of this paper is available from Elsevier at:
<http://dx.doi.org/10.1016/j.cmpb.2017.08.009>

Title

A method for generating 3D thermal models with decoupled acquisition

Author names and affiliations

Andriy Guilherme Krefer <andriy.krefer@gmail.com>⁽¹⁾

Maiko Min Ian Lie <minian.lie@gmail.com>⁽¹⁾

Gustavo Benvenutti Borba <gustavobborba@utfpr.edu.br>⁽²⁾

Humberto Remigio Gamba <humberto@utfpr.edu.br>⁽¹⁾

Marcos Dinís Lavarda <marcos.dinis.lavarda@gmail.com>⁽²⁾

Mauren Abreu de Souza <mauren.abreu.souza@gmail.com>⁽²⁾

(1) Graduate School on Electrical Engineering - CPGEI, Department of Electronics - DAELN, Federal University of Technology - Paraná - UTFPR, Av. Sete de Setembro 3165, 80230-901, Curitiba, Paraná, Brazil.

(2) Graduate School on Biomedical Engineering - PPGBE, Department of Electronics - DAELN, Federal University of Technology - Paraná - UTFPR, Av. Sete de Setembro 3165, 80230-901, Curitiba, Paraná, Brazil.

Concise abstract: This work presents a method for generation of 3D thermal models that allows combination of separately acquired 3D mesh and thermal images. Among the advantages of this decoupling are increased modularity of acquisition procedures and reuse of legacy equipment and data. Unlike previous methods, it is considered that the 3D mesh and the thermal images are acquired separately, so camera pose estimation is required to determine the correct spatial positioning from which to project the images. As thermal images of human skin are predominantly homogeneous, an intensity transformation is proposed to increase the efficacy of interest point detection and make the approach feasible. For validation of the method, the design and implementation of a test object is presented. It can be used to validate other methods and can be reproduced with common printed circuit board manufacturing processes. The proposed approach is accurate, with an average displacement error of 1.41 mm ($s = 0.74$ mm) with the validation test object and 4.58 mm ($s = 2.12$ mm) with human subjects.

Keywords: Multi-modality imaging, 3D thermography, Structure from Motion, Scale Invariant Feature Transform

A method for generating 3D thermal models with decoupled acquisition

Abstract

Background and Objective: Both thermal imaging and 3D scanning offer convenient advantages for medical applications, namely, being contactless, non-invasive and fast. Consequently, many approaches have been proposed to combine both sensing modalities in order to acquire 3D thermal models. The predominant approach is to affix a 3D scanner and a thermal camera in the same support and calibrate them together. While this approach allows straightforward projection of thermal images over the 3D mesh, it requires their simultaneous acquisition. In this work, a method for generation of 3D thermal models that allows combination of separately acquired 3D mesh and thermal images is presented. Among the advantages of this decoupled acquisition are increased modularity of acquisition procedures and reuse of legacy equipment and data.

Methods: The proposed method is based on the projection of thermal images over a 3D mesh. Unlike previous methods, it is considered that the 3D mesh and the thermal images are acquired separately, so camera pose estimation is required to determine the correct spatial positioning from which to project the images. This is done using Structure from Motion, which requires a series of interest points correspondences between the images, for which the SIFT method was used. As thermal images of human skin are predominantly homogeneous, an intensity transformation is proposed to increase the efficacy of interest point detection and make the approach feasible. Before projection, the adequate alignment of the 3D mesh in space is determined using Particle Swarm Optimization. For validation of the method, the design and implementation of a test object is presented. It can be used to validate other methods and can be reproduced with common printed circuit board manufacturing processes.

Results: The proposed approach is accurate, with an average displacement error of 1.41 mm ($s = 0.74$ mm) with the validation test object and [4.58 mm \(\$s = 2.12\$ mm\)](#) with human subjects.

Conclusions: The proposed method is able to combine separately acquired 3D mesh and thermal images into an accurate 3D thermal model. The results with human subjects suggest that the method can be successfully employed in medical applications.

Keywords: Multi-modality imaging, 3D thermography, Structure from Motion, Scale Invariant Feature Transform.

1 Introduction

Infrared thermography is a technique that allows estimating the temperature of an object from its infrared emission. As every object with temperature above the absolute zero emits infrared radiation, this sensing modality is widely applicable and has been adopted in contexts such as generation of photorealistic models of architectural monuments [1], industrial inspection [2], clothing design [3], among many others [4]. One application domain of particular interest is medical diagnosis, where the contactless, non-invasive and fast measurements of infrared thermography are especially desirable. There are several applications of thermography in medical diagnosis, ranging from sports medicine, in which pre and post-activity temperatures are monitored to diagnose thermoregulatory abnormalities [5, 6], to cancer diagnosis, in which, for instance, temperature is monitored over time to distinguish benign and malign pigmented lesions [7, 8, 9]. In fact, any condition that influences skin surface temperature can benefit from infrared thermography analysis, including tuberculin reaction [10], stress [11], not to mention blunt trauma and other forensic applications such as time of death estimation [12].

Another sensing modality that has been increasingly adopted in medical applications is 3D scanning (i.e. range imaging). It allows shape and size measurements while sharing the above mentioned conveniences of infrared thermography [13]. Among its medical applications are deformity detection, skin analysis [13] and plastic surgery planning [14]. 3D models also allow 3D printing – the production of haptic physical models by addition of physical layers – which can be used for treatment planning, training, construction of customized prosthetics, among other applications [15, 16].

Considering the similar advantages and complementary measurement information of 2D thermography and 3D scanning, several approaches for their combined application have been proposed [17, 18, 19, 20]. This multi-modality sensing method – 3D thermography – enhances temperature analysis with geometrical information and vice-versa, improving, for instance, diagnosis of Diabetic Foot Disease (DFD) which involve monitoring both blood circulation (i.e. temperature) and ulcer evolution (i.e. surface shape) [18]. Existing 3D thermography approaches are mostly based on the integration of a thermal camera and a 3D scanner in a single instrument by affixing them in the same structural support – a stand [17, 18, 19] or a hand-held mechanism [20]. The former approach is more common in medical diagnosis settings, where the environment is more easily controlled and precise data acquisition guidelines can be employed [21]. The latter is usually applied in industrial settings [20], where the environment has a fixed configuration and the sensing device must adequate itself to its constraints. The aforementioned methods are characterized by the simultaneous acquisition of both 2D thermal and 3D range data. This offers the advantage of straightforward data combination as both sensing devices can be calibrated together, however, the necessity of simultaneous acquisition is also a significant

limitation.

This paper presents a 3D thermography method for medical applications, which is based on the projection of a series of thermal images over a 3D mesh, generating a 3D thermal model – without the necessity of simultaneous acquisition of 2D and 3D data, unlike previous methods. Among the advantages of this decoupling are modularization of the acquisition procedures and the possibility of legacy equipment reuse. As 3D scanning technologies expand a wide range of accuracy/cost trade-off and different sensing modalities can be offered by different clinics, a decoupled and more modular acquisition process allows easy adaption to different time and cost circumstances. Moreover, this approach also allows reuse of previously acquired data, as long as adequate data acquisition guidelines are followed to maintain similar acquisition conditions.

The projection of thermal images over a 3D mesh, in methods that acquire data from both sensing modalities simultaneously, is trivial [18]. On the other hand, camera pose estimation is required when data acquisition is decoupled, as is the case in this work. This is done using Structure from Motion (SfM), which requires a series of interest point matches between images from different perspectives [22]. Due to the low-resolution and homogeneous aspect of thermal images, which hinders interest point detection, this approach has been unexplored in thermography. To address this, an image intensity transformation is presented, which significantly improves interest point detection in thermal images and allows a sufficient number of matches for adequate camera pose estimation. The thermal images are projected from the estimated poses over the 3D mesh, which is aligned through an optimization model solved via Particle Swarm Optimization (PSO), resulting in the final 3D thermal model.

A validation of the method is presented using a test object, called Heat Texture Test Object (HTTO), for which the motivation, design and evaluation is also described. Additionally, a case study with human subjects, with quantitative evaluation, is presented to demonstrate the applicability of the method in the context of medical diagnosis. The results show that the approach successfully generates accurate 3D thermal models, presenting average displacement error of 1.41 mm ($s = 0.74$ mm) for the test object and **4.58 mm ($s = 2.12$ mm)** for the human subjects.

The remainder of this paper is organized as follows. Section 2 shows a general overview of the proposed method, followed by a detailed explanation of its stages. Section 3 describes the design and implementation of the HTTO, including the experiments used to determine its adequate characteristics. Section 4 presents qualitative and quantitative evaluation of the proposed method on the HTTO and on human subjects, with a discussion of the obtained results. Section 6 concludes this work, indicating future improvements and research directions.

2 Proposed Method

The proposed method is capable of projecting 2D thermal images of an object onto its respective 3D mesh, which does not need to be acquired simultaneously with the thermal images. Figure 1 describes the main steps of the proposed method, which are detailed as follows.

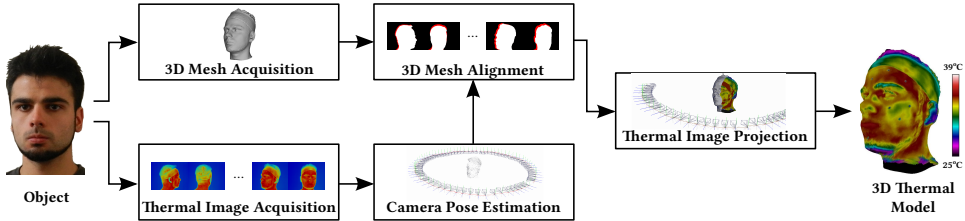


Figure 1: Overview of the proposed method.

2.1 3D Mesh Acquisition

For the acquisition of the 3D mesh, a Creaform 3D Gemini scanner was used – it has a resolution of 0.4 mm in the X and Y axes and of 0.2 mm in the Z axis. The manufacturer’s recommendation is for the acquisition to be made from a distance of approximately one meter from the object [23]. To obtain the complete mesh, the acquisition must be made from several angles. The respective patches are registered to form a single 3D object using the ICP (Iterative Closest Point) algorithm [24] through the Geomagic software.

2.2 Thermal Image Acquisition

For the acquisition of the thermal images, a FLIR infrared camera model A325 was used. It is sensitive to wavelengths of 7.5 to 13 μm and can record temperatures from -20 to 120 °C with a thermal resolution of 0.05 °C, at 30 frames per second with a resolution of 320×240 pixels [25]. The lens used has a nominal focal length of 18 mm.

During the thermography experiments, it was observed that long periods in the acquisition of the images caused significant temperature variations on the skin surface. To address this, a rotating system (Figure 2) was designed and assembled to allow faster and more accurate acquisition of the thermal images. The system provides adjustment of distance d , height h , and angulation of the thermal camera (i.e. α , β , θ and γ).

A motor with speed control coupled to the rotation axis ω (ranging from 0 to 360°) allows capturing images at multiple angles while maintaining a fixed distance d to the object. The acquisition of all thermal images was conducted in a room with an especially built air-conditioner that allows control of temperature and humidity variations, and air circulation.

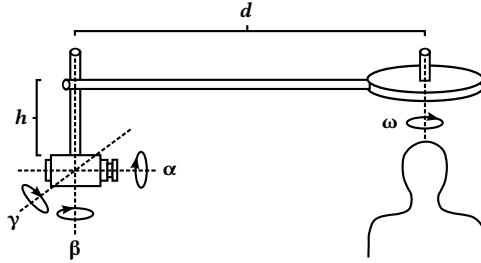


Figure 2: Swivel stand for thermal image acquisition.

The acquired sequence of thermal images is exported to the CSV (Comma Separated Values) format using the FLIR Tools 4.0 software. Obtained values are expressed in degrees Celsius, with each value representing a pixel of the image. CSV files are then converted to PNG image format using MATLAB. A selection of 70 thermal images, captured at uniformly spaced angles and fixed distance from the object, was adopted for projection onto the 3D mesh.

2.3 Camera Pose Estimation

Structure from Motion (SfM) is a process that simultaneously estimates the 3D structure of an object and the camera poses during image acquisition. In general, Bundle Adjustment (BA) is used for this purpose [26], while SfM is a more general term that aggregates the whole set of techniques used. Since thermal images typically have a low resolution and do not actually describe geometry information, the 3D structure output from SfM is not accurate or reliable enough for our purposes. Consequently, the 3D structure is acquired from a 3D scanner, as described in Section 2.1, while SfM is used only for camera pose estimation. For this purpose, a minimal number of correspondences between image points, acquired from multiple viewpoints, is required. These correspondences are obtained using detection, description and matching of interest points in these images.

Thermal images of human skin do not have as much details as their corresponding visible light images. There are no abrupt variations in temperature, thus, they tend to be more homogeneous [27]. This characteristic makes the detection and matching of interest points difficult [18, 28, 29]. Considering this, and the fact that SfM was originally designed for visible light images, a pre-processing step was devised to adequate thermal images for this process. A transformation $m(T)$ is proposed on the intensity levels T of the thermal image (normalized in the $[0, 255]$ range), in order to increase the number of regions with high-contrast texture and, consequently, the number of interest points detected. The transformation $m(T)$ is described in Equation 1:

$$m(T) = \frac{255}{2} \left(1 - \cos \left(\frac{2\pi f T}{255} \right) \right), \quad (1)$$

in which f is an adjustable parameter that is determined empirically for our experiments ($f = 3.5$). This transformation creates artificial contrasts in the intensity levels of the image, emphasizing variations that were previously too subtle to be detected, consequently, increasing the number of interest points detected. At first, the usefulness of such artificial variations might seem dubious for interest point matching, given that images captured at different instants and from different perspectives will hardly maintain the same intensities for the corresponding locations – making these additional interest points poor candidates for matching. However, even though this is the case for visible light images, it is not the case for thermal images. The effect of illumination in the acquisition of different images is irrelevant for thermal images, since it does not cause any significant variation in temperature. Thus, even though the transformation described in Equation 1 creates artificial contrasts, it does not have any significant negative effect on matching, given that the created contrasts are consistent between different thermal images. Figure 3 shows the effect of the intensity transformation described by Equation 1 on a thermal image – it significantly increases the number of interest points detected.

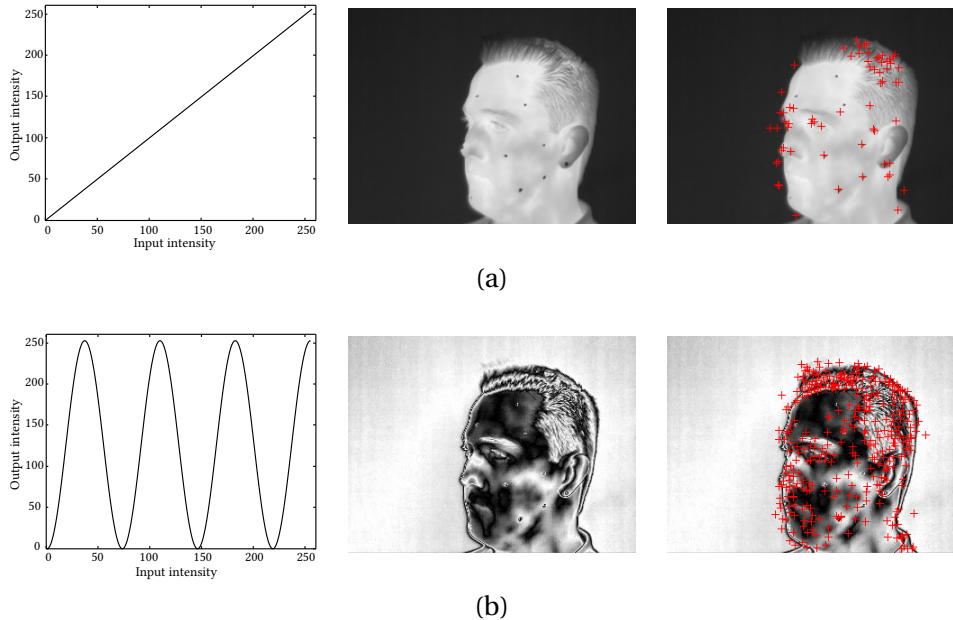


Figure 3: Effect of the intensity transformation on interest point detection (in red) in thermal images. The images are shown with a grayscale palette to facilitate the interpretation of the transformation. (a) Original intensity levels. (b) Transformed intensity levels.

The detection and description of interest points is done using the SIFT (Scale Invariant Feature Transform) method [30] through the SiftGPU software [31] and the VisualSfM interface [32]. The matching between interest points in the different images is made with the nearest point based on the Euclidean distance be-

tween their descriptors, that is, an interest point in an image is matched with the point in another image which minimizes the Euclidean distance between their SIFT descriptors. The inconsistent matches are then filtered through RANSAC (Random Sample Consensus) [33].

With the set of consistent matches, it is possible to estimate the camera poses through Bundle Adjustment, using the Parallel Bundle Adjustment (PBA) software [34]. Additionally, it is possible to significantly improve the precision of pose estimation by incorporating the internal parameters of the camera – the intrinsic matrix \mathbf{K} , described in Equation 2:

$$\mathbf{K} = \begin{pmatrix} f_x & a_x & c_x & 0 \\ a_y & f_y & c_y & 0 \\ 0 & 0 & 1 & 0 \\ 0 & 0 & 0 & 1 \end{pmatrix} = \begin{pmatrix} 720 & 0 & 160 & 0 \\ 0 & 720 & 120 & 0 \\ 0 & 0 & 1 & 0 \\ 0 & 0 & 0 & 1 \end{pmatrix}. \quad (2)$$

The matrix \mathbf{K} is previously computed and is the same for all poses, since all thermal images were captured by the same camera. At last, determining the camera poses consists in the computation of the extrinsic matrix \mathbf{G} , described by Equation 3:

$$\mathbf{G} = \mathbf{R}_x^{-1} \cdot \mathbf{R}_y^{-1} \cdot \mathbf{R}_z^{-1} \cdot \mathbf{T}_x^{-1} \cdot \mathbf{T}_y^{-1} \cdot \mathbf{T}_z^{-1}, \quad (3)$$

in which the matrices $\mathbf{R}_{\{x,y,z\}}^{-1}$ and $\mathbf{T}_{\{x,y,z\}}^{-1}$ are, respectively, the inverses of the rotation and translation matrices in three dimensions.

Figure 4 shows the pose estimation and the obtained sparse point cloud. Figures 4 (a) and (b) show the pose estimation without and with the previous calculation of the intrinsic matrix, respectively. Knowing that the swivel stand was used for acquisition of the thermal images and that the camera performed a circular movement around the subject, it is possible to notice that, with the intrinsic matrix, the real positioning of the camera is estimated much more accurately (Figure 4 (b)).

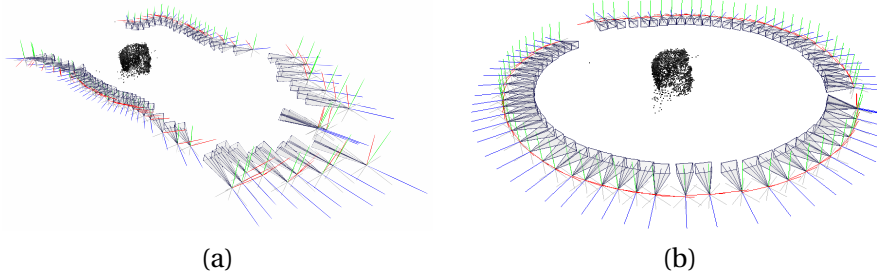


Figure 4: Camera pose estimation. (a) Without initialization of the intrinsic matrix. (b) With initialization of the intrinsic matrix.

2.4 3D Mesh Alignment

For an adequate projection of the thermal images onto the 3D mesh, the mesh must be aligned in the same plane of the camera. The desired alignment is the one that minimizes the overlap error between the thermal image and the two-dimensional rendering of the 3D model. The rendering of the 3D model in a specific pose is determined by the transformation described in Equation 4:

$$p_{out} = K \cdot G \cdot p_{in}, \quad (4)$$

in which p_{in} is a point in the model, K and G are the intrinsic and extrinsic matrices of the camera, respectively.

To determine overlap error, the rendering R of the 3D model and the thermal image T are thresholded to segment the object of interest, resulting in binary images R_T and T_T . The overlap error Err is the number of pixels that indicate the object in one of the images but not in both – the pixels in which the segmentation in the two images do not overlap, as described in Equation 5:

$$Err(R_T, T_T) = (R_T \cup T_T) - (R_T \cap T_T). \quad (5)$$

Figure 5 illustrates overlap error, in which red and orange pixels correspond to the segmentation of the object in the rendering of the 3D model and in the thermal image, respectively, while the white pixels indicate the overlap between the segmentation of both images. The error is the sum of the number of red and orange pixels.



Figure 5: Overlap error between the rendering of the 3D model and the thermal image. They are indicated by white, red and orange, respectively.

From function Err , that measures the error (i.e. the quality of the alignment), the appropriate determination of the alignment can be modeled as an optimization problem. For its solution, Particle Swarm Optimization (PSO), which is a swarm-based metaheuristic algorithm [35], was adopted. The choice of this algorithm was motivated by the fact that it presents the shortest convergence time in the benchmark performed by Vesterstrom and Thomsen (2004) [36]. The PSO searches the solution space for a vector with seven elements related to the

alignment of the 3D model, i.e. $(x, y, z, \theta, \rho, \phi, s)^T$, the first three elements corresponding to position, the next three to rotation and the last one to scale.

At each iteration of the PSO, the overlap between the rendering of the 3D model with the thermal image is done for each of the 70 previously estimated poses (i.e. intrinsic and extrinsic matrices). The accumulated error for all poses characterizes the performance of the current alignment – PSO searches for the solution which minimizes this error.

2.5 Thermal Image Projection

After aligning the 3D mesh, thermal images are projected onto its surface using the MeshLab software [37]. Due to the relatively large number of thermal images projected (i.e. 70), there is a significant number of superimpositions. Thus, the color value attributed to each point of the 3D model is a weighted average of these projections, in which the contribution of each thermal image is proportional to the distance of the camera to the point and of the point to the center of the image (Figure 6).

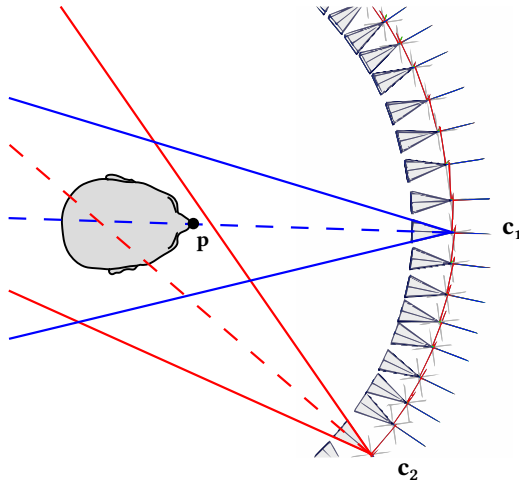


Figure 6: Projection of the thermal images on the 3D mesh. Pose c_1 is closer to the point p than pose c_2 . The point p is also closer to the center of the image (dashed line) in pose c_1 than in pose c_2 . Consequently, the contribution of the projection c_1 in p is greater than the contribution of c_2 .

3 Heat Texture Test Object

A test object was designed to validate the general idea of the proposed approach, providing an approximation of “ideal” conditions. In addition to demonstrating that the proposed approach is feasible, it provides a baseline with which to compare the results obtained on the more difficult case of human subject data.

The validation of the proposed method requires a test object with the following requirements:

- i The object must be three-dimensional: the aim of the proposed method is to combine a 3D model with thermal images, thus the test object must be a 3D object;
- ii The object must be capable of significant thermal emission: the aim of the proposed method is to combine a 3D model with thermal images, thus the test object must emit enough heat for it to be visible to the thermal camera;
- iii The object must be non-deformable: the shape of the object must be stable during the 3D model and thermal image acquisition, otherwise, it may not be possible to distinguish whether errors in the fusion were due to the quality of the data or the method;
- iv The object must have rich thermal texture: the proposed method depends on interest point detection using the SIFT method, which detects them as extrema in scale space. These extrema do not occur in homogeneous regions, thus a thermal texture is required for detection of an appropriate number of interest points.

A test object, called HTTO – Heat Texture Test Object, with the above described properties was assembled for validation of the proposed method. Its design is based on double layer fiberglass FR-4 printed circuit boards (PCBs) arranged as a parallelepiped. In each board, on the layer which is internal to the parallelepiped, PCB tracks were distributed in a closely spaced zigzag pattern (described in more detail below) to approximate an uniform thermal emission when powered. The layer on the exterior of the parallelepiped has a thermal marker texture, so that when the internal layer emits heat, it propagates through regions with only PCB fiberglass, while reflecting on regions with thermal marker, thus making a distinguishable pattern when viewed by a thermal camera. This double layer approach allows arbitrary textures, since the external layer does not need to conduct electricity.

3.1 Thermal Characteristics of PCB Elements

Before building the HTTO, a series of tests were performed in a double-layer fiberglass FR-4 PCB. The test board has an area of $15.2 \text{ cm} \times 10.1 \text{ cm}$, and copper layers with thickness of $35 \mu\text{m}$. The layers of the board were divided into 9 regions, shown in Figure 7, with different thermal conductor configurations and materials. The four regions dedicated to evaluation of the heating emission by different conductor configurations are labeled as R1, R7, R8 and R9 – implemented in a zigzag pattern, as illustrated in Figure 8. The considered configurations are: *chessboard* (each square has an area of 1 cm^2), *various* and

uniform (with and without silkscreen). *Chessboard* is used in several popular tools [38] that implement calibration techniques based on the study by Zhang [39]. *Various* and *uniform* are variations of the *chessboard* pattern.

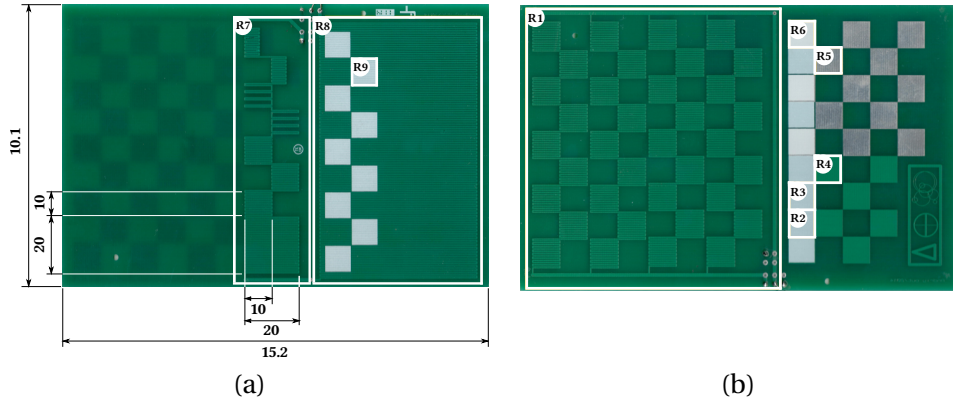


Figure 7: PCB for evaluation of thermal characteristics – measurements are in millimeters. Each of the nine regions implements a thermal conductor configuration or a different material combination. (a) Top layer. (b) Bottom layer.

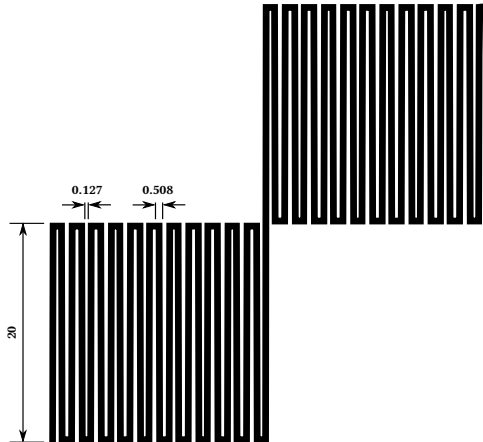


Figure 8: Tracks in the implementation of patterns in the evaluation PCB. Measurements are in millimeters.

Table 1 presents the configurations in each region of the PCB. Regions dedicated to the evaluation of different combinations of materials are R2-R6, the combinations are described in Table 2. Only materials which are common in the manufacture of PCBs were considered (i.e. copper, tin-plating, varnish, silkscreen), allowing easy reproduction by usual manufacturing processes. The objective of this preliminary study was to determine the best track configurations and materials that provide an effective thermal marker for the HTTO.

Figure 9 shows the thermal images of regions R1, R7, R8 and R9. The heating of the region R1 results in a blurred thermal image as can be seen in Fig-

Table 1: Thermal conductor configurations of the evaluation PCB.

Region	Conductor configuration
R1	Chessboard
R7	Various
R8	Uniform
R9	Uniform with silkscreen

Table 2: Combinations of materials for the thermal conductors of the evaluation PCB. Note that, due to the specific sequence employed in usual manufacturing processes, there are some combinations that are unviable and were not considered.

Region	Materials
R2	Varnish, silkscreen
R3	Copper, varnish, silkscreen
R4	Copper, varnish
R5	Tin-plated copper
R6	Tin-plated copper, silkscreen

ure 9 (a). The heating of region R7 , Figure 9 (b), shows that sparser patterns simply dissipate less heat, and the *various* configurations are not distinguishable. The evaluation of the thermal images of regions R8 and R9 were done by heating from region R8, since R9 is simply a subregion of R8 with an additional silkscreen coating. As can be seen in Figure 9 (c), there is no significant difference in the heat emission of a uniform region with or without silkscreen. There is heat concentration in the upper portion of region R8, which occurs due to the heat reflectivity of the chess pattern of region R5, on the opposite layer. This occurrence demonstrates that it is possible to heat the conductor even without the application of electric current on it, through the application of current in the conductor on the opposite layer.

Regions dedicated to the evaluation of the different combinations of materials are R2-R6, the combinations are described in Table 2. Only materials which are common in the manufacture of PCBs were considered (i.e. copper, tin-plating, varnish, silkscreen), allowing easy reproduction by usual manufacturing processes. Figure 10 presents the thermal images of regions R1-R6, obtained with electrical current conduction on the opposite layer. The viability of this heating method was observed previously, during the evaluation of the electrical conductor configurations.

It is possible to note that, except for region R5, no combination of materials allows a well-defined identification of the pattern by the thermal camera. PCB fiberglass areas covered only by varnish dissipate heat, while areas covered only

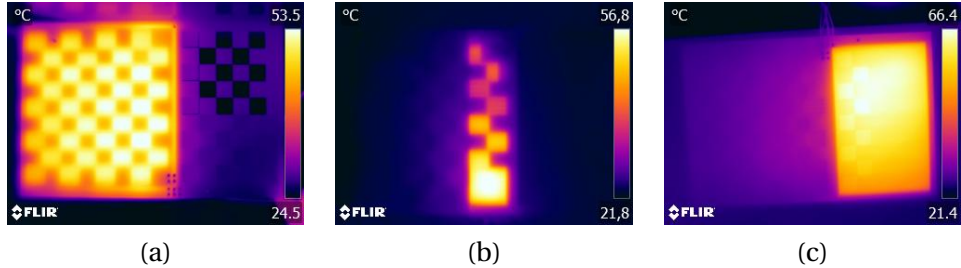


Figure 9: Heat emission for the different configurations of the electric/thermal conductor. (a) R1 – Chessboard (bottom layer). (b) R7 – Various (top layer). (c) R8, R9 – Uniform (top layer).

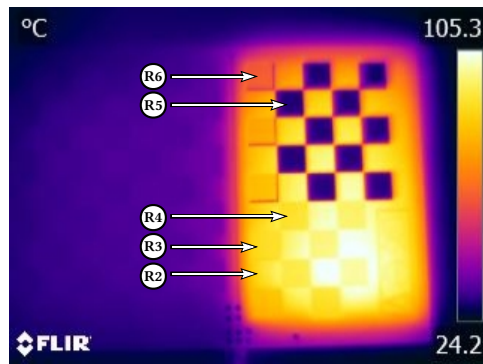


Figure 10: Heat emision for different combination of materials.

by tin-plated copper (i.e. R5) effectively block it, allowing a clear distinction between them. This result suggests that varnish causes significant heat distribution, interfering excessively in the distinction of the patterns by the thermal camera. The silkscreen interferes less than varnish, but only marginally (i.e. the region appears slightly darker), as can be seen by the heating in region R6. Thus, we consider the use of tin-plated copper as the most suitable for implementation of the thermal texture.

3.2 HTTO Design and Assembly

The HTTO was designed and assembled based on the thermal characteristics observed in the experiment described in the previous section. The specifications of the assembled object are presented below in terms of the requirements, which were presented previously, and the specifications that fulfill these requirements.

- i The object must be three-dimensional: the PCBs that compose the test object were arranged in the form of a parallelepiped, with surface dimensions of $10 \times 15 \text{ cm}$ and $10 \times 10.32 \text{ cm}$, as shown in Figure 11;

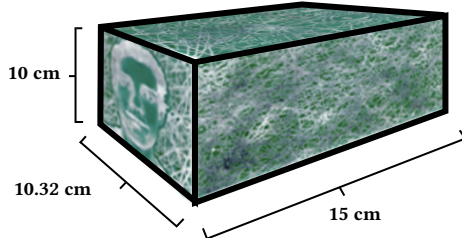


Figure 11: Measurements of the assembled HTTO. The PCBs are disposed as a parallelepiped.

- ii The object must be capable of significant thermal emission: from the thermal characteristics observed in the experiments described in Section 3.1, tin-plated copper patterns were incorporated in the external layers of the PCBs, while the parallelepiped internal layers have a zigzag pattern of uniform conductor configuration. The zigzag tracks in the internal layer are electrically powered and effectively heat the surface of the object. As the frontal/posterior and lateral PCBs have different sizes, the electrical resistance of their tracks are also different. Considering this, the resistances of the tracks in each board were measured and they were powered with proportional voltages, so that they dissipate the same power and, consequently, have approximately the same temperature;
- iii The object must be nondeformable: the HTTO is composed of fiberglass (FR-4) boards affixed with silicone, presenting rigid structure;
- iv The object must have rich textures thermal: dense and heterogeneous patterns of tin-plated copper have been elaborated for the external surface of the object. The patterns used in the manufacture of the PCBs are shown in Figure 12.

4 Results

In this section, the evaluation results of the proposed approach with the HTTO are presented. An assessment of the proposed intensity transformation is made on thermal images of human subjects, to quantify the increase in interest point detection and their robustness under different measurements. An assessment of 3D thermal models obtained with the proposed method on human subjects is also presented, in order to demonstrate its applicability under conditions similar to those present in medical applications.

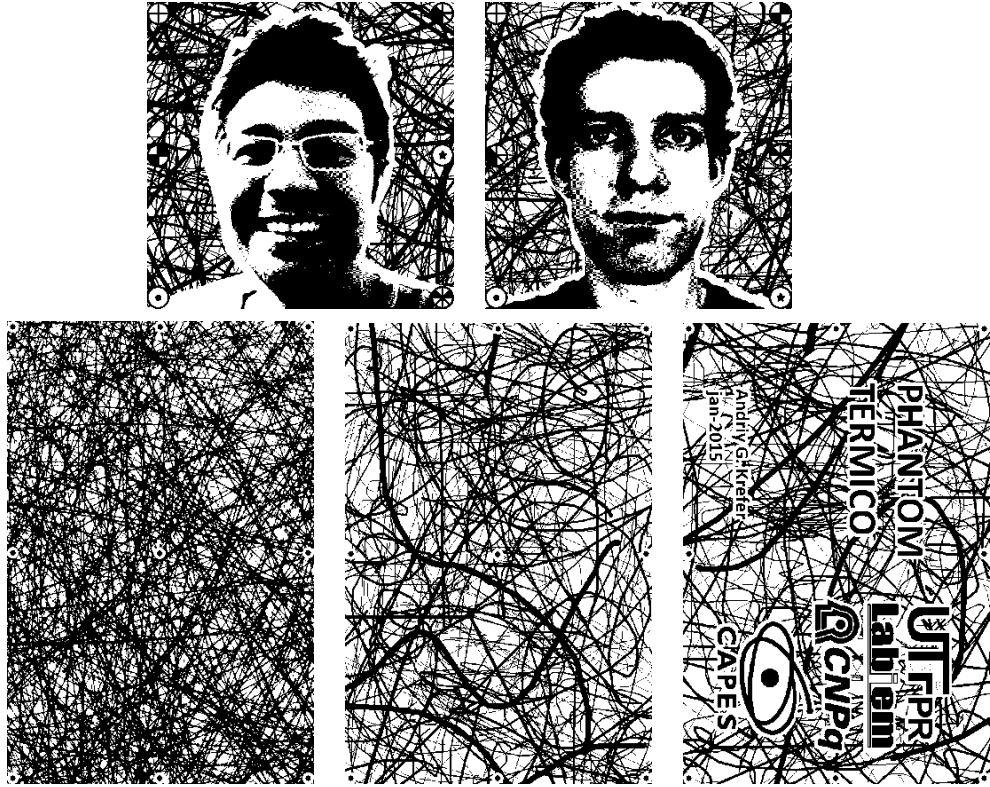


Figure 12: Copper patterns of the external surface of the HTTO – there are only five surfaces because the bottom of the parallelepiped is hollow. Top row: surfaces F₁, F₂. Bottom row: surfaces F₃, F₄ and F₅.

4.1 Method Validation

The method validation consists in assessing the displacement error between the manually projected reference, comprised of the images in Figure 12, and the automatically projected thermal images using the proposed method. Since the parallelepiped has flat sides, the error can be easily evaluated per-surface as the 2D error of the matched interest points themselves.

Figure 13 (a) shows the manual projection of the PCB layout, shown in Figure 12, over a parallelepiped 3D mesh. The simulated mesh has the HTTO specified dimensions. Figure 13 (a) is the measurement reference. Figure 13 (b) shows the thermal image projection over the same simulated mesh using the proposed method. The thermal projections around the sides of the mesh are close to the reference, but two aspects are noticeable. First, the top surface has a significantly distorted projection. This is consequence of the procedure adopted for thermal image acquisition, in which the camera translates around the test object over a single plane, causing occlusion in regions of the object that are not visible from the sides. Since this problem can be solved by acquisition of images

at additional angles, we consider that it does not compromise the validity of the method, as it contemplates the possibility of such acquisitions using the mechanism described in Figure 2 – therefore the evaluation follows without considering the top surface of the HTTO (F_5 in Figure 12). Second, the thermal texture presents less details than the PCB layout. This loss of fine detail is due to the low resolution of the thermal images (i.e. 320×240). Although this aspect impacts the interest point detection, it does not compromise the method because enough interest points are detected, albeit in reduced quantity. To illustrate this, the interest point detection, matching and filtering is presented in Figure 14.

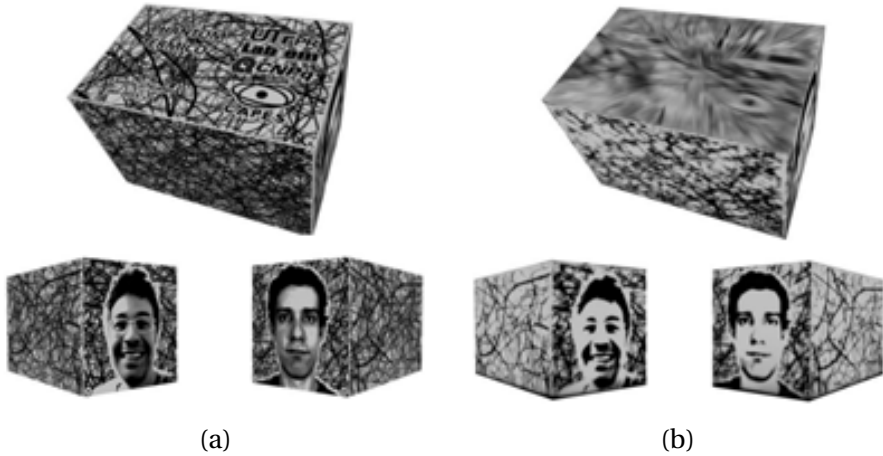


Figure 13: Qualitative evaluation of the proposed method on the HTTO. (a) Ideal 3D model. (b) Thermal projection using the proposed method. The images are shown with a grayscale palette to facilitate comparison with the reference.

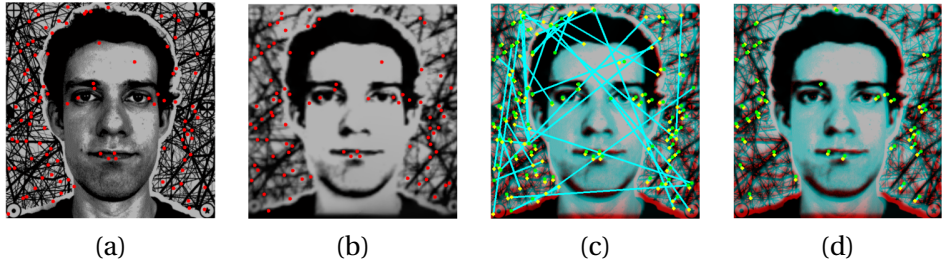


Figure 14: Validation of the proposed method – interest point matching for the surface F_2 of the HTTO. Interest points for the individual images are indicated in red, matches in yellow and matching error in cyan (lines). (a) Interest points in the PCB layout. (b) Interest points in the thermal image. (c) Matches. (d) Matches after RANSAC.

In Figure 14, a series of incorrect matches can be noticed. They were already expected, as evidenced by experiments in stereoscopic vision and 3D reconstruction methods [33]. To address this the matches are filtered using RANSAC. Table 3 summarizes the results of the interest point detection and matching.

Table 3: Number of interest points and matches in the HTTO.

Surface	Interest points		Matches	Matches after RANSAC
	Layout	Thermal		
F ₁	3686	759	138	53
F ₂	4014	761	112	42
F ₃	10521	2141	102	38
F ₄	13980	2554	139	57

Considering that a significant number of interest point matches remain, the displacement error between the interest points can be evaluated. A summary of the displacement error for each surface of the HTTO is presented in Table 4, in which it is possible to notice that the method is accurate, with a maximum error of 3.73 mm.

Table 4: Matching error between interest points in the HTTO.

Surface	Avg. error (pixels)	Avg. error (mm)	St. dev. (mm)	Min. Error (mm)	Max. error (mm)
F ₁	7.43	1.54	1.02	0.06	3.73
F ₂	7.71	1.61	0.68	0.46	2.76
F ₃	6.24	1.33	0.31	0.45	1.97
F ₄	5.42	1.16	0.58	0.24	2.78
Total	6.70	1.41	0.74	0.06	3.73

4.2 Intensity Transformation

Recall that unlike the HTTO, which was designed to display rich thermal textures, human skin has a much more homogeneous aspect on thermal images. To address this, an intensity transformation was proposed (Equation 1), which significantly increases the number of interest points detected in such images. To illustrate the improvement resulting from this transformation, Figure 15 shows some examples of interest point detection on thermal images of the human subjects, without and with the transformation. For subjects S₁₋₄, the intensity transformation increased the number of interest points detected approximately eight (from 54 to 434), ten (from 42 to 460), six (from 57 to 357), and nine (from 34 to 318) times, respectively.

The robustness of the proposed intensity transformation was assessed in terms of number of correct matches under varying viewpoint angles. The reference image (i.e. viewpoint angle of 0°) corresponds to a frontal image of the

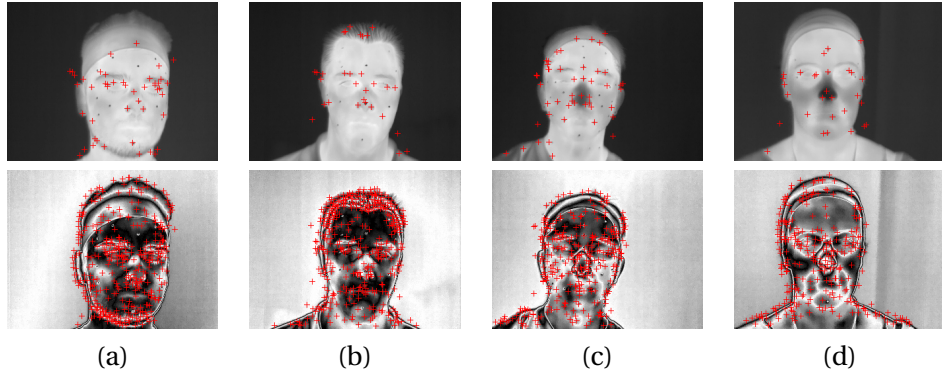


Figure 15: Effect of the proposed intensity transformation on interest point detection in thermal images. The images are shown with a grayscale palette to facilitate interpretation of the transformation. Top row: without transformation. Bottom row: with transformation. From left to right: subjects S₁, S₂, S₃, and S₄.

face. Four sets of thermal images were acquired, with a delay of approximately three minutes between each set, to account for temperature variation under a time frame plausible for thermal image acquisition. There was a maximum variation of 3°C between the average temperature of the image sets. Figure 16 shows the results of the experiment with and without the transformation. The transformation clearly improves performance, very significantly. From the number of matches under a small viewpoint angle (e.g. 5°), it is possible to notice that the results from Figure 15 are indeed representative, since both indicate a performance increase of approximately ten times.

As expected, with the intensity transformation, the number of correct matches decreases rapidly with increasing viewpoint changes, which is reasonable, since the most distinctive (i.e. more stable keypoints are detected) regions of the head occur in the frontal view of the face. Without the transformation the decrease is more subtle, since there are almost no matches.

4.3 Case Study with Human Subjects

In order to demonstrate the use of the proposed method in medical applications, experiments were made with two human subjects. The simple geometry of the HTTO allowed evaluation on a per-surface basis. Additionally, the entire surface texture was a thermal marker by design, so that 2D displacement error between matching interest points could be used to estimate projection error. None of these is true for human subjects – markers must be manually placed for error measurement.

For each subject, markers that are both visually and thermally visible – fiducial markers – were placed on their faces during 3D mesh and thermal image acquisition, so that their displacement in the visible (i.e. mesh with visible light texture) and thermal 3D models could be measured at these locations. Note that

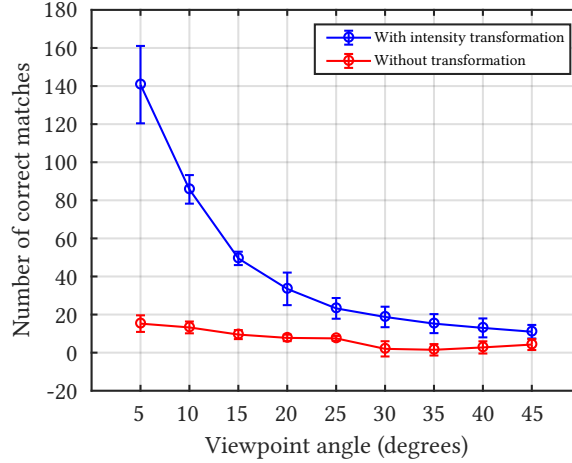


Figure 16: Number of correct matches under varying viewpoint angles. Error bars indicate standard deviation. Four sets of thermal images (each contemplating viewpoint angles in the 5° – 45° range) were considered, with a delay of approximately three minutes between the acquisition of each set. There was a maximum variation of approximately 3°C between the average temperature of the image sets.

the visible light texture is used only for evaluation, since the markers are not geometrically distinctive – the proposed method itself has no need for it. Moreover, the 3D thermography was restricted to the head, as it has representative applications such as in dentistry (e.g. temporomandibular disorders [40]) and facial recognition [19, 41].

In each 3D model, nine markers were placed at the positions indicated in Figure 17. The displacement error of the markers was measured as their Euclidean distance, presented in Table 5.

Table 5: Displacement error for the fiducial markers in the visible light and thermal 3D models.

Subject	Avg. error (mm)	St. dev. (mm)	Min. Error (mm)	Max. error (mm)
S ₁	3.69	1.45	1.94	5.81
S ₂	5.64	2.17	1.69	9.87
S ₃	4.57	1.79	2.19	7.45
S ₄	4.41	2.87	1.73	8.74
Total	4.58	2.12	1.69	9.87

The average error (i.e. 4.58 mm) is reasonable, especially considering that the average head circumference of an adult male with average height (i.e. 1600 mm – 1800 mm) is approximately 600 mm [42], and that the markers themselves

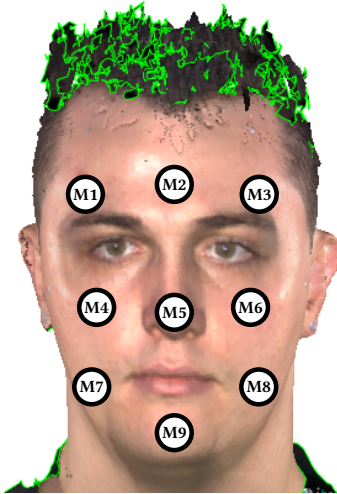


Figure 17: Fiducial marker positioning.

had a 3 mm diameter. The largest error (i.e. 9.87 mm) occurs in the marker on the nose of subject S₂. It might seem like a large error compared to the maximum obtained with the HTTO, but considering that it accounts for three dimensions, unlike with the HTTO, in which the error is two-dimensional (it was accounted for each surface), it is reasonably small. Nevertheless, this error is not negligible and suggests that the simple weighted average approach described in Section 3 might be improved – even though it is enough to show the efficacy of the proposed method. Figure 18 shows, from different views, the 3D thermographs output by the proposed method. Overall, the results clearly show that the method is effective, despite the higher error compared to those observed in the evaluation with the HTTO.

As discussed in the evaluation of the HTTO, there might be imperfections related to areas of occlusion that occur during the acquisition of the thermal images. This issue is noticeable, for instance, in the regions of the 3D thermal model corresponding to the chin of subject S₁ (Figure 19). Again, these areas of occlusion are consequence of the circular motion of the thermal camera during thermal image acquisition. Because this motion is done in a single plane around the middle segment of the head, segments above and below are subject to occlusion. This issue can be solved simply by acquiring images at additional angles, i.e. varying h and γ in the swivel stand described in Figure 2.

5 Discussion

The analysis of displacement error showed that the proposed method is accurate under the simplified conditions provided by the HTTO. In this manner, it not only validates the general approach of the proposed method, but also pro-

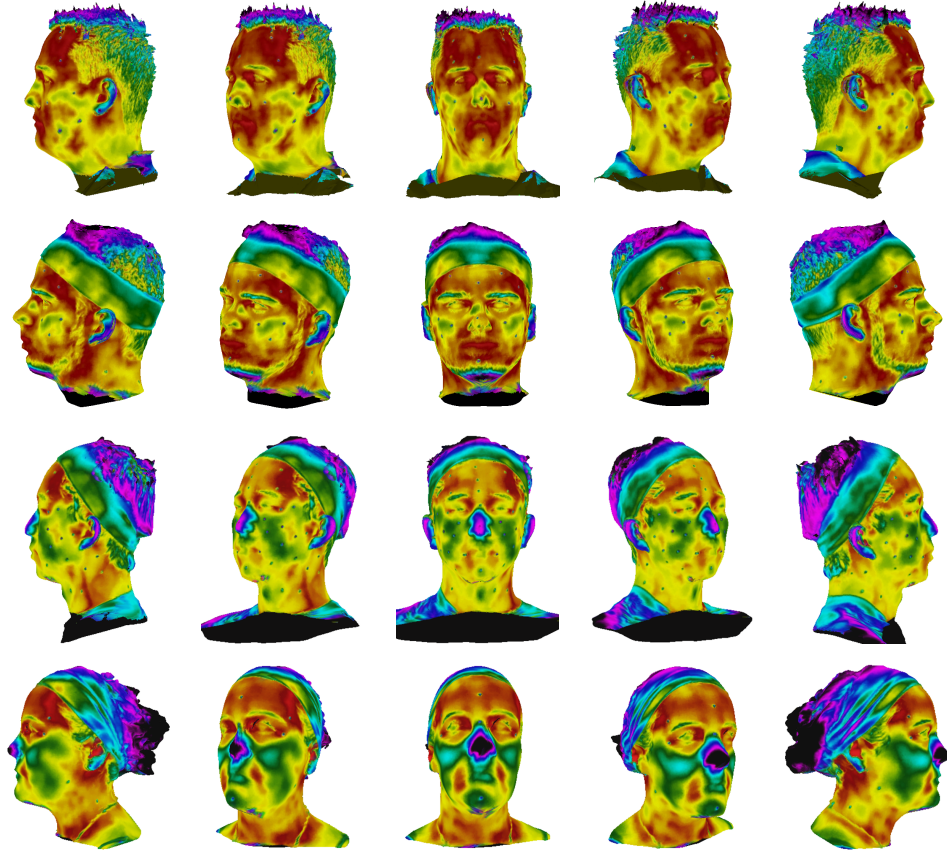


Figure 18: 3D thermal models obtained using the proposed method. From top to bottom row: subjects S₁, S₂, S₃, S₄.

vides a baseline for comparison of the results obtained with human subjects. Compared to using the HTTO, there are two main difficulties when employing the proposed approach on human subjects: poor contrast and significantly more complex geometry. To handle poor contrast, an intensity transformation was proposed, which was shown to increase very significantly the number of interest points detected. An assessment of the number of correct matches under varying viewpoint angles showed that the proposed transformation not only achieves consistently superior performance with respect to the original thermal images, but that it is robust under different measurements. Despite being more challenging, the more complex geometry did not compromise the process, since the local planarity of human faces were enough to detect an adequate number of stable interest points.

With an adequate number of stable interest points, camera pose estimation and 3D mesh alignment can be adequately employed for thermal image projection. The 3D thermal model resulting from this processing pipeline was shown

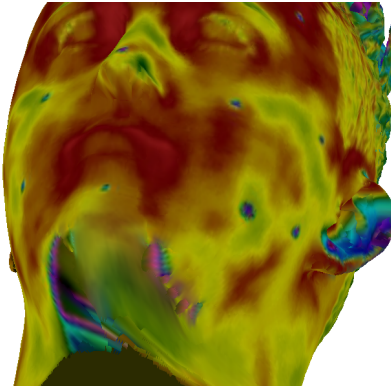


Figure 19: Imperfections in the 3D thermal model due to areas of occlusion during thermal image acquisition.

to be accurate through an assessment of displacement error of fiducial markers. Taking the low resolution of the thermal images (i.e. 320×240) and diameter of the markers (i.e. 3 mm) into account, the errors are remarkably small. The projection might present some local errors under occluded regions (e.g. subject chin) of the thermal camera setup, but these can be mitigated by acquisitions of thermal images from additional angles.

Our approach differs from most other works that focus on biomedical applications, in which the common approach to compute 3D thermal models is to simultaneously acquire 3D geometry and 2D thermal data by affixing them together [17, 18, 20, 43]. In this case, thermal image projection into a 3D model is straightforward, since both imaging modalities are calibrated together. Some authors have even employed this approach for augmented reality, using a real projector to project thermal data over the physical object [44]. Our results show that such restrictive acquisition conditions can be avoided by employing pose estimation via Structure from Motion, as long as the thermal images are subject to an adequate intensity transformation.

A framework similar to ours was proposed in the context of Nondestructive Testing and Evaluation (NDT&E) applications by Akhloufi and Verney [45]. Their framework employs a projection of thermal data over a 3D height map, which relies on matching features over both imaging modalities. Since thermal data (and in this case, even the height map) have very low-contrast, the authors employ contrast stretching for dynamic range enhancement. In comparison, our work presents the following advantages. First, our approach does not rely on markers for feature detection. Fiducial markers are employed only for assessment of displacement error – the thermal image with intensity transformation is enough for feature detection. Second, our intensity transformation is capable of generating much more contrast than simple contrast stretching, so that the SIFT descriptor can be employed. This results in more robustness than the Hough transform employed by Akhloufi and Verney [45], which must assume the shape

of the content to be detected. Additionally, their assessment is qualitative, while we provide a quantitative analysis in terms of amount and robustness of interest points detected, as well as displacement error in the thermal projection over the 3D mesh.

6 Conclusions

This paper presented a 3D thermography method that does not require coupled acquisition of 3D mesh and thermal images, unlike previous methods. Such decoupling allows more modular acquisition processes, which have advantages such as legacy equipment and data reuse. The method is based on camera pose estimation through Structure from Motion (SfM), which is widely employed for visible light images, but not so on thermal images. The issue with thermal images, namely, the lack of texture for adequate interest point detection, was addressed with an intensity transformation that increased the number of detections up to ten-fold in experiments with human subjects. For the validation of the proposed method, the design and implementation of the HTTO (Heat Texture Test Object) was presented. The HTTO can be easily reproduced with common printed circuit board manufacturing processes and can be used to evaluate other methods of 3D mesh and thermal image fusion. An evaluation of the proposed method on the HTTO showed that it is very accurate, resulting in an average displacement error of 1.41 mm ($s = 0.74$ mm). Additionally, the method was evaluated with human subjects in order to demonstrate its applicability under medical application conditions, resulting in an average displacement error of 4.58 mm ($s = 2.12$ mm), showing that the proposed method is also accurate with human subjects. Future work includes precise procedures to eliminate occlusion areas, improvement in the way the thermal projections are used (i.e. weighted average) to decrease displacement error, and evaluating the method with other interest point detectors and descriptors.

References

- [1] Miriam Cabrelles, Sergio Galcerá, Santiago Navarro, José Luis Lerma, Talal Akasheh, and Naif Haddad. Integration of 3D Laser Scanning, Photogrammetry and Thermography to Record Architectural Monuments. In *Proceedings of the 22nd International CIPA Symposium*, page 6, 2009.
- [2] W. Harvey Gray, Christophe Dumont, and Mongi A. Abidi. Integration of Multiple Range and Intensity Image Pairs Using a Volumetric Method to Create Textured 3D Models. *Proceedings of the SPIE*, 3966:94–104, 2000.
- [3] Tanya Domina, Patrick Kinnicutt, and Maureen MacGillivray. Thermal Pattern Variations Analyzed Using 2D/3D Mapping Techniques Among Fe-

- males. *Journal of Textile and Apparel, Technology and Management*, 7(1), 2011.
- [4] B.B. Lahiri, S. Bagavathiappan, T. Jayakumar, and John Philip. Medical Applications of Infrared Thermography: A Review. *Infrared Physics & Technology*, 55(4):221 – 235, 2012.
 - [5] Joseph Costello, Ian B Stewart, James Selfe, Anne I Karki, and Alan Donnelly. Use of Thermal Imaging in Sports Medicine Research: a Short Report. *International SportMed Journal*, 14(2):94–98, 2013.
 - [6] Carolin Hildebrandt, Karlheinz Zeilberger, Edward Francis John Ring, and Christian Raschner. The Application of Medical Infrared Thermography in Sports Medicine. *Ultrasound*, 10:2, 2012.
 - [7] M. Pirtini Çetingül and C. Herman. Quantification of the Thermal Signature of a Melanoma Lesion. *International Journal of Thermal Sciences*, 50(4):421 – 431, 2011.
 - [8] Tiago B. Borchartt, Aura Conci, Rita C.F. Lima, Roger Resmini, and Angel Sanchez. Breast Thermography from an Image Processing Viewpoint: A survey . *Signal Processing*, 93(10):2785 – 2803, 2013.
 - [9] L. F Silva, D. C. M. Saade, G. O. Sequeiros, A. C. Silva, A. C. Paiva, R. S. Bravo, and A. Conci. A New Database for Breast Research with Infrared Image. *Journal of Medical Imaging and Health Informatics*, 4(1):92–100, 2014.
 - [10] José Antonio Fiz, Manuel Lozano, Enrique Monte-Moreno, Adela Gonzalez-Martinez, Marcos Faundez-Zanuy, Caroline Becker, Laura Pons-Rodriguez, and Juan Ruiz Manzano. Tuberculin Reaction Measured by Infrared Thermography. *Computer Methods and Programs in Biomedicine*, 122(2):199 – 206, 2015.
 - [11] Nandita Sharma and Tom Gedeon. Objective Measures, Sensors and Computational Techniques for Stress Recognition and Classification: A Survey. *Computer Methods and Programs in Biomedicine*, 108(3):1287 – 1301, 2012.
 - [12] K. Ammer and E. F. J. Ring. Application of Thermal Imaging in Forensic Medicine. *The Imaging Science Journal*, 53(3):125–131, 2005.
 - [13] Philip Treleaven and J. C. K. Wells. 3D Body Scanning and Healthcare Applications. *Computer*, 40(7):28–34, 2007.
 - [14] Michael R. Markiewicz and R. Bryan Bell. The use of 3d imaging tools in facial plastic surgery. *Facial Plastic Surgery Clinics of North America*, 19(4):655 – 682, 2011. 3D Imaging Technologies for Facial Plastic Surgery.

- [15] F. Rengier, A. Mehndiratta, H. von Tengg-Kobligk, C. M. Zechmann, R. Unterhinninghofen, H.-U. Kauczor, and F. L. Giesel. 3D Printing Based on Imaging Data: Review of Medical Applications. *International Journal of Computer Assisted Radiology and Surgery*, 5(4):335–341, 2010.
- [16] Seongjin Park, Ho Chul Kang, Jeongjin Lee, Juneseuk Shin, and Yeong Gil Shin. An Enhanced Method for Registration of Dental Surfaces Partially Scanned by a 3D Dental Laser Scanning. *Computer Methods and Programs in Biomedicine*, 118(1):11 – 22, 2015.
- [17] Pavel Aksенов, Iain Clark, David Grant, Alan Inman, Leor Vartikovski, and Jean christophe Nebel. 3D Thermography for Quantification of Heat Generation Resulting from Inflammation. In *Proceedings of the 3D Modeling Symposium*, 2003.
- [18] S. Barone, A. Paoli, and A. V. Razionale. A Biomedical Application Combining Visible and Thermal 3D Imaging. In *Proceedings of the XVIII International Congress on Graphics Engineering*, pages 1–9, 2006.
- [19] R. Yang and Y. Chen. Design of a 3-D Infrared Imaging System Using Structured Light. *IEEE Transactions on Instrumentation and Measurement*, 60(2):608–617, Feb 2011.
- [20] S. Vidas, P. Moghadam, and S. Sridharan. Real-Time Mobile 3D Temperature Mapping. *IEEE Sensors Journal*, 15(2):1145–1152, Feb 2015.
- [21] Ismael Fernández-Cuevas, Joao Carlos Bouzas Marins, Javier Arnáiz Lastras, Pedro María Gómez Carmona, Sergio Pi nonosa Cano, Miguel Ángel García-Concepción, and Manuel Sillero-Quintana. Classification of Factors Influencing the Use of Infrared Thermography in Humans: A Review. *Infrared Physics & Technology*, 71:28 – 55, 2015.
- [22] Noah Snavely, Steven M. Seitz, and Richard Szeliski. Photo Tourism: Exploring Photo Collections in 3D. *ACM Transactions on Graphics*, 25(3):835–846, July 2006.
- [23] Legacy Products | Discontinued Products | Gemini | Creaform. <http://www.creaform3d.com/en/customer-support/legacy-products/gemini>, 2016. Accessed: 2016-12-02.
- [24] Yang Chen and Gérard Medioni. Object Modelling by Registration of Multiple Range Images. *Image and Vision Computing*, 10(3):145 – 155, 1992.
- [25] FLIR A325sc Infrared Camera Datasheet. http://www.flirmedia.com/MMC/THG/Brochures/RND_010/RND_010_US.pdf, 2016. Accessed: 2016-12-02.

- [26] Bill Triggs, Philip F. McLauchlan, Richard I. Hartley, and Andrew W. Fitzgibbon. Bundle Adjustment – A Modern Synthesis. In *Proceedings of the International Workshop on Vision Algorithms*, pages 298–372. Springer, 1999.
- [27] Y. Yun and I. Y. H. Gu. Multi-view Face Pose Classification by Boosting with Weak Hypothesis Fusion Using Visual and Infrared Images. In *Proceedings of the IEEE International Conference on Acoustics, Speech and Signal Processing (ICASSP)*, pages 1949–1952, March 2012.
- [28] Youngjib Ham and Mani Golparvar-Fard. An Automated Vision-based Method for Rapid 3D Energy Performance Modeling of Existing Buildings Using Thermal and Digital Imagery. *Advanced Engineering Informatics*, 27(3):395 – 409, 2013.
- [29] Yong K. Cho, Youngjib Ham, and Mani Golpavar-Fard. 3D as-is Building Energy Modeling and Diagnostics: A Review of the State-of-the-Art. *Advanced Engineering Informatics*, 29(2):184 – 195, 2015.
- [30] David G. Lowe. Distinctive Image Features from Scale-Invariant Keypoints. *International Journal of Computer Vision*, 60(2):91–110, 2004.
- [31] SiftGPU: A GPU Implementation of Scale Invariant Feature Transform (SIFT). <http://cs.unc.edu/~ccwu/siftgpu>, 2016. Accessed: 2016-12-02.
- [32] C. Wu. Towards Linear-Time Incremental Structure from Motion. In *Proceedings of the International Conference on 3D Vision*, pages 127–134, June 2013.
- [33] Martin A. Fischler and Robert C. Bolles. Random Sample Consensus: A Paradigm for Model Fitting with Applications to Image Analysis and Automated Cartography. *Communications of the ACM*, 24(6):381–395, June 1981.
- [34] C. Wu, S. Agarwal, B. Curless, and S. M. Seitz. Multicore bundle adjustment. In *Proceedings of the IEEE Conference on Computer Vision and Pattern Recognition (CVPR)*, pages 3057–3064, June 2011.
- [35] Russ C. Eberhart and James Kennedy. A New Optimizer Using Particle Swarm Theory. In *Proceedings of the Sixth International Symposium on Micro Machine and Human Science*, 1995.
- [36] J. Vesterstrom and R. Thomsen. A Comparative Study of Differential Evolution, Particle Swarm Optimization, and Evolutionary Algorithms on Numerical Benchmark Problems. In *Proceedings of the Congress on Evolutionary Computation (CEC)*, volume 2, pages 1980–1987 Vol.2, June 2004.
- [37] Paolo Cignoni, Marco Callieri, Massimiliano Corsini, Matteo Dellepiane, Fabio Ganovelli, and Guido Ranzuglia. MeshLab: an Open-source Mesh

- Processing Tool. In *Proceedings of the Eurographics Conference, Italian Chapter*, volume 2008, pages 129–136, 2008.
- [38] Jean-Yves Bouguet. Camera calibration toolbox for MATLAB. http://www.vision.caltech.edu/bouguetj/calib_doc/, 2016. Accessed: 2015-05-20.
 - [39] Z. Zhang. A Flexible new Technique for Camera Calibration. *IEEE Transactions on Pattern Analysis and Machine Intelligence*, 22(11):1330–1334, Nov 2000.
 - [40] Mauren Abreu de Souza, Andriy G. Krefer, Gustavo B. Borba, Gustavo J. Vizinoni e Silva, Ana Paula G. O. Franco, and Humberto R. Gamba. Generation of 3D Thermal Models for Dentistry Applications. In *2016 38th Annual International Conference of the IEEE Engineering in Medicine and Biology Society (EMBC)*, pages 1397–1400, Aug 2016.
 - [41] Sunjin Yu, Joongrock Kim, and Sangyoun Lee. Thermal 3D Modeling System Based on 3-view Geometry. *Optics Communications*, 285(24):5019 – 5028, 2012.
 - [42] K. M. Bushby, T. Cole, J. N. Matthews, and J. A. Goodship. Centiles for Adult Head Circumference. *Archives of Disease in Childhood*, 67(10):1286–1287, 1992.
 - [43] G. Chernov, V. Chernov, and M. Barboza Flores. 3D Dynamic Thermography System for Biomedical Applications. In Eddie YK Ng and Mahnaz Etehad tavakol, editors, *Application of Infrared to Biomedical Sciences*, pages 517–545. Springer Singapore, Singapore, 2017.
 - [44] D. Borrman, F. Leutert, K. Schilling, and A. Nüchter. Spatial Projection of Thermal Data for Visual Inspection. In *Proceedings of the International Conference on Control, Automation, Robotics and Vision*, pages 1–6, Nov 2016.
 - [45] Moulay A. Akhloufi and Benjamin Verney. Multimodal Registration and Fusion for 3D Thermal Imaging. *Mathematical Problems in Engineering*, 2015(450101):1–14, July 2015.